

ARMY RESEARCH LABORATORY



Generalized Wideband Harmonic Imaging of Nonlinearly Loaded Scatterers: Theory, Analysis, and Application for Forward-Looking Radar Target Detection

by DaHan Liao

ARL-TR-7121

September 2014

NOTICES

Disclaimers

The findings in this report are not to be construed as an official Department of the Army position unless so designated by other authorized documents.

Citation of manufacturer's or trade names does not constitute an official endorsement or approval of the use thereof.

Destroy this report when it is no longer needed. Do not return it to the originator.

Army Research Laboratory

Adelphi, MD 20783-1138

ARL-TR-7121

September 2014

Generalized Wideband Harmonic Imaging of Nonlinearly Loaded Scatterers: Theory, Analysis, and Application for Forward-Looking Radar Target Detection

DaHan Liao

Sensors and Electron Devices Directorate, ARL

REPORT DOCUMENTATION PAGE				Form Approved OMB No. 0704-0188
<p>Public reporting burden for this collection of information is estimated to average 1 hour per response, including the time for reviewing instructions, searching existing data sources, gathering and maintaining the data needed, and completing and reviewing the collection information. Send comments regarding this burden estimate or any other aspect of this collection of information, including suggestions for reducing the burden, to Department of Defense, Washington Headquarters Services, Directorate for Information Operations and Reports (0704-0188), 1215 Jefferson Davis Highway, Suite 1204, Arlington, VA 22202-4302. Respondents should be aware that notwithstanding any other provision of law, no person shall be subject to any penalty for failing to comply with a collection of information if it does not display a currently valid OMB control number.</p> <p>PLEASE DO NOT RETURN YOUR FORM TO THE ABOVE ADDRESS.</p>				
1. REPORT DATE (DD-MM-YYYY) September 2014	2. REPORT TYPE Final	3. DATES COVERED (From - To) 2013–2014		
4. TITLE AND SUBTITLE Generalized Wideband Harmonic Imaging of Nonlinearly Loaded Scatterers: Theory, Analysis, and Application for Forward-Looking Radar Target Detection		5a. CONTRACT NUMBER		
		5b. GRANT NUMBER		
		5c. PROGRAM ELEMENT NUMBER		
6. AUTHOR(S) DaHan Liao		5d. PROJECT NUMBER		
		5e. TASK NUMBER		
		5f. WORK UNIT NUMBER		
7. PERFORMING ORGANIZATION NAME(S) AND ADDRESS(ES) US Army Research Laboratory ATTN: RDRL-SER-U 2800 Powder Mill Road Adelphi, MD 20783-1138		8. PERFORMING ORGANIZATION REPORT NUMBER ARL-TR-7121		
9. SPONSORING/MONITORING AGENCY NAME(S) AND ADDRESS(ES)		10. SPONSOR/MONITOR'S ACRONYM(S)		
		11. SPONSOR/MONITOR'S REPORT NUMBER(S)		
12. DISTRIBUTION/AVAILABILITY STATEMENT Approved for public release; distribution unlimited.				
13. SUPPLEMENTARY NOTES				
14. ABSTRACT Wideband electromagnetic sensing and imaging of nonlinearly loaded scatterers is considered. Harmonic scattering theory is first presented, and then a generalized near-field, direct imaging functional is proposed for free-space and near-ground target localization within the context of forward-looking radar standoff detection exploiting sequential single-tone excitation. The developed scattering and imaging analysis framework is illustrated for point-like and extended targets through numerical experiments performed with a hybrid method-of-moments solver, in conjunction with a harmonic balance approach and an asymptotic field propagation technique. The steady-state harmonic scattering responses are examined in the time, frequency, and image domains for scatterers in free-space and half-space environments, and accurate target localization is demonstrated in all cases for each harmonic order considered.				
15. SUBJECT TERMS Computational electromagnetics, radar scattering and imaging, harmonic scattering, wideband, nonlinear loaded scattering				
16. SECURITY CLASSIFICATION OF:		17. LIMITATION OF ABSTRACT	18. NUMBER OF PAGES	19a. NAME OF RESPONSIBLE PERSON
A. Report Unclassified	b. ABSTRACT Unclassified	c. THIS PAGE Unclassified	UU 26	DaHan Liao 19b. TELEPHONE NUMBER (Include area code) (301) 394-1741

Contents

List of Figures	iv
1. Introduction	1
2. Theoretical Background	2
3. Numerical Experiments	5
3.1 Harmonic Scattering Characterization	5
3.2 Imaging Results and Discussions	6
4. Conclusions	16
5. References	17
Distribution List	20

List of Figures

Fig. 1 Standoff sensing of nonlinearly loaded scatterer.....	3
Fig. 2 Harmonic imaging results for diode-loaded, free-space point-like target: a) $ \Psi_1(\mathbf{r}) $; b) $ \Psi_2(\mathbf{r}) $; c) $ \Psi_3(\mathbf{r}) $; and d) $ \Psi_4(\mathbf{r}) $. F = [300 MHz, 1.5 GHz], transmitted power = 10 W.....	7
Fig. 3 Normalized time-domain harmonic scattering responses for diode-loaded, free-space extended target: a) n = 1; b) n = 2; c) n = 3; and d) n = 4.....	9
Fig. 4 Normalized time-domain harmonic scattering responses for diode-loaded, on-surface extended target: a) n = 1; b) n = 2; c) n = 3; and d) n = 4.....	10
Fig. 5 Normalized time-domain harmonic scattering responses for diode-loaded, subsurface extended target: a) n = 1; b) n = 2; c) n = 3; and d) n = 4.....	11
Fig. 6 Frequency-domain harmonic scattering responses for diode-loaded extended target for n = 1,2,3,4: a) free-space; b) on-surface; and c) subsurface.....	12
Fig. 7 Harmonic imaging results for diode-loaded, free-space extended target: a) $ \Psi_1(\mathbf{r}) $; b) $ \Psi_2(\mathbf{r}) $; c) $ \Psi_3(\mathbf{r}) $; and d) $ \Psi_4(\mathbf{r}) $. F = [300 MHz, 1.5 GHz], transmitted power = 10 W.....	13
Fig. 8 Harmonic imaging results for diode-loaded, on-surface extended target: a) $ \Psi_1(\mathbf{r}) $; b) $ \Psi_2(\mathbf{r}) $; c) $ \Psi_3(\mathbf{r}) $; and d) $ \Psi_4(\mathbf{r}) $. F = [300 MHz, 1.5 GHz], transmitted power = 10 W.....	14
Fig. 9 Harmonic imaging results for diode-loaded, subsurface extended target: a) $ \Psi_1(\mathbf{r}) $; b) $ \Psi_2(\mathbf{r}) $; c) $ \Psi_3(\mathbf{r}) $; and d) $ \Psi_4(\mathbf{r}) $. F = [300 MHz, 1.5 GHz], transmitted power = 10 W.....	15

1. Introduction

For route clearance and force protection, one technology of acute interest to the military is the standoff detection of targets using electromagnetic waves. An implementation of the technology in the form of the forward-looking radar (FLR) has been discussed in various studies^{1–5} within the context of in-road and roadside threat detection. A conventional FLR system—whether operating in, for example, impulse, step-frequency, or frequency-modulated continuous-wave (FMCW) mode—employs ultra-wideband signals to probe and—subsequently—image a scene by exploiting linear scattering responses. Since many prominent classes of targets encountered in theater are electronics-based and give off nonlinear re-radiated responses, recently there has been increased impetus in developing a nonlinear complement to the linear FLR. Nonlinear electromagnetic sensing—possessing its own unique set of implementation challenges notwithstanding—could potentially provide an additional mode of detection and has certain advantages compared to traditional radar technologies. For example, nonlinear detection can be leveraged to aid the extraction of a nonlinear target embedded in linear manmade or natural clutter; and analysis of the target harmonic re-emissions can lead to further opportunities in signature and image classification. The above discussions demonstrate there is the need for understanding the scattering properties of—as well as developing new imaging algorithms for—nonlinear targets and hence establish the motivation for the current study.

The concept of nonlinear radar has been explored within the radio-frequency identification (RFID) community: associated applications range from insect tracking⁶ to inventory tagging,^{7,8} wherein localization is usually achieved through direction-of-arrival and time-of-arrival techniques. The subject of nonlinear electromagnetic scattering has been investigated extensively.^{9–25} These works are pertinent to the modeling of nonlinearly loaded antennas, though it is conceivable that the analysis in these studies can be generalized to treat any nonlinearly loaded scatterer; unfortunately, the remote sensing aspect of the problem is not considered in detail—that is, these works do not discuss the exploitation of the harmonic scattering responses for target detection, localization, and imaging. A recent study²⁶ presented a comprehensive numerical solver for characterizing the multistatic harmonic responses of nonlinearly loaded antenna targets under tone excitation in the presence of a half-space, and thence, proposed a subspace-based direct imaging technique for near-field location estimation of on-surface and buried targets. Image construction in that work is achieved not by wideband beamforming but rather by processing the “narrowband” scattered fields in the subspace domain at a single harmonic or multiple harmonics. The numerical experiment-derived imaging results reported²⁶ indicate that while accurate target localization—and even “super-resolution”—can be obtained using an aspect-limited transceiver aperture consistent with that of the FLR, the

imaging performance can be rather noise sensitive—which is typical of subspace-based methods. Note that the imaging algorithm described in that work necessitates the use of a fully multistatic scattered field matrix, which may not always be convenient to generate in practical sensing systems.

The current study is envisioned as a companion to the previous study,²⁶ with the focus on wideband imaging: more to the point, the objective here is to establish a wideband imaging framework based on the nonlinear scattering response that is directly complementary to the one based on the linear scattering response. The algorithm is expected to be equally applicable to all common sensing modes of interest—these include the fully multistatic configuration, as well as monostatic and bistatic ones. The presentation of this work is organized as follows. In Section 2, the conceptual underpinnings of nonlinear scattering theory and the harmonic imaging algorithm are first discussed. Then, in Section 3, numerical experiments are performed to illustrate the nonlinear FLR sensing problem as pertinent to step-frequency systems: viz., in Section 3.1, simulations are carried out using the previous scattering and propagation solver²⁶ and, in Section 3.2, standoff harmonic imaging results—and interpretations thereof—are put forth for point-like and extended scatterers in free-space and half-space environments. Finally, in Section 4, a summary of this work is given.

2. Theoretical Background

The scene (Fig. 1) with the target (a nonlinearly loaded, perfectly conducting scatterer) is assumed to be excited by infinitesimal electric dipoles at \mathbf{r}' transmitting time-harmonic fields at evenly spaced frequencies $f \in F = \{f_1, f_2, \dots, f_p\}$. Given an induced Norton equivalent short-circuit current $I_{sc}(f) \rightarrow i_{sc}(t) = a \cos(2\pi ft + \theta)$, the resultant voltage at the scatterer terminal is of the form

$$v_s(t) = \sum_{n=0}^{\infty} \alpha_n(f, a) [\cos(2\pi ft + \theta)]^n = \sum_{n=0}^{\infty} \beta_n(f, a) \cos(2\pi nft + n\theta). \quad (1)$$

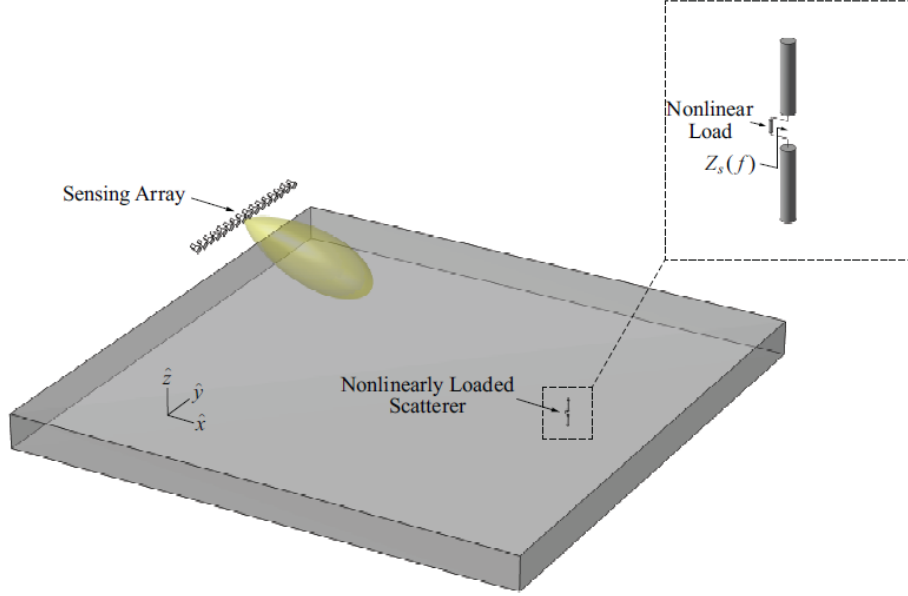


Fig. 1 Standoff sensing of nonlinearly loaded scatterer

For small signals, $\beta_n(f, a) \approx a^n \gamma_n(f)$. The dependence of the purely real variables $\alpha_n(f, a)$, $\beta_n(f, a)$, and $\gamma_n(f)$ on the scatterer impedance $Z_s(f)$ and the current-voltage ($i - v$) characteristic of the load ($i(t) = g(v(t))$) is implicit and hence suppressed.

For each instance of excitation at frequency f , the target generates harmonic scattered fields $E_s(\mathbf{r}, \mathbf{r}', nf)$ at frequencies nf ($n \neq 0$): for $n = 1$, the steady-state scattered field is the sum of the structural mode $E_{s,0}(\mathbf{r}, \mathbf{r}', f)$ —that is, the response from the scatterer when it is short-circuited—and the re-radiation mode $E_{s,r}(\mathbf{r}, \mathbf{r}', f)$; for $n > 1$, only the re-radiation mode $E_{s,r}(\mathbf{r}, \mathbf{r}', nf)$ exists. The re-radiation mode is evaluated by exciting the scatterer with voltage source $V_s(nf)$ at the terminal,²⁶ where $V_s(nf)$ is the phasor representation for the signal component of Eq. 1 with frequency nf .

For a point-like target at \mathbf{r}_s , the structural mode can be written as

$$E_{s,0}(\mathbf{r}, \mathbf{r}', f) = G(\mathbf{r}, \mathbf{r}_s, f) \ell_{s,0}(f) G(\mathbf{r}_s, \mathbf{r}', f) \ell_{TX}(f), \quad (2)$$

where $\ell_{TX}(f)$ is the current moment of the transmitter, $\ell_{s,0}(f)$ is the scattering strength of the short-circuited target, and $G(\cdot, \cdot, f)$ is the Green's function of the environment; the term $G(\mathbf{r}_s, \mathbf{r}', f) \ell_{TX}(f)$ can be interpreted as equivalent to a scalar incident field $E_{inc}(\mathbf{r}_s, \mathbf{r}', f)$. The re-radiation mode can be deduced as follows. First, the short-circuit current is approximated as

$$I_{sc}(f) = \ell_e(f) G(\mathbf{r}_s, \mathbf{r}', f) \ell_{TX}(f), \quad (3)$$

in which $\ell_e(f)$ is the scalar effective length²⁷ of the scatterer as defined by exciting the terminal with a voltage source. Then from Eq. 1, it can be shown that $V_s(nf) = \beta_n(f, |I_{sc}(f)|) e^{jn\angle I_{sc}(f)}$. In turn, the re-radiated field is

$$E_{s,r}(\mathbf{r}, \mathbf{r}', nf) = V_s(nf) G(\mathbf{r}, \mathbf{r}_s, nf) \ell_r(nf) = \beta_n(f, |I_{sc}(f)|) e^{jn\angle I_{sc}(f)} G(\mathbf{r}, \mathbf{r}_s, nf) \ell_r(nf), \quad (4)$$

with $\ell_r(nf)$ as the induced current moment at the scatterer due to a unity voltage source placed at the terminal. In view of Eqs. 2–4, a phase conjugation approach is proposed to obtain an imaging functional to locate the target at each harmonic order n :

$$\Psi_n(\mathbf{r}) = \sum_{TX} \sum_{RX} \sum_F W(f) E_s(\mathbf{r}, \mathbf{r}', nf) \left[G(\mathbf{r}_s, \mathbf{r}', f)^n G(\mathbf{r}, \mathbf{r}_s, nf) \right]^*, \quad (5)$$

where TX and RX , respectively, represent the transmitter and receiver array spaces (which are assumed to be collocated), $W(f)$ is a spectral window function, and $*$ denotes the conjugation operation. The above imaging functional is not limited to only low-power (small-signal) operations; it is general enough so that it can accommodate high-power (large-signal) sensing as well—which may be needed to detect targets with very weak nonlinear scattering.

The point spread function characteristics of Eq. 5 for free-space and near-ground (on-surface and shallow-buried) targets can be derived by following the procedure documented previously.²⁸ The FLR sensing geometry (see Fig. 1) affords rather poor resolution in the vertical—or elevation—direction, so the predominant issue of interest here is the behavior of the point spread function across the horizontal plane. In the forward-looking—or broadside—direction, assuming a rectangular spectral window, the first-null down-range and angular cross-range resolutions of $\Psi_n(\mathbf{r})$, respectively, can be shown to be

$$\delta r = \frac{1}{n} \frac{c_o}{2\Delta f}; \quad (6)$$

$$\delta\phi = \frac{1}{n} \frac{\lambda_{c,o}}{2L}; \quad (7)$$

where c_o is the velocity of the electromagnetic wave in free-space; Δf is the bandwidth of F ; $\lambda_{c,o}$ is the wavelength at the center frequency of F ; and L is the width of the transceiver array aperture. The results from Eqs. 6 and 7 are valid for a monostatic sensing geometry as well as a bistatic configuration with two end-transmitters (i.e., one transmitter located at each end of the array and receiving over the entire aperture). For a fully multistatic system or a bistatic system

with only one transmitter, Eq. 6 still holds, but the cross-range resolution is twice of that stated in Eq. 7. A tapered spectral window can be applied to suppress the sidelobes in range—at the expense of degrading the down-range resolution. In practice, note that depending on the nature of the window and the sensing configuration, the cross-range imaging behavior could also be affected. It is important to emphasize that the formulations for the resolution and the observations given above are equally valid for both free-space and near-ground target imaging.

In general, for a non-point-like—or extended—target and an arbitrary vector incident field, Eqs. 3 and 4 should be modified, respectively, as

$$I_{sc}(f) = \mathbf{E}_{inc}(\mathbf{r}_s, \mathbf{r}', f) \cdot \ell_e(f); \quad (8)$$

and

$$\mathbf{E}_{s,r}(\mathbf{r}, \mathbf{r}', nf) = \beta_n(f, |I_{sc}(f)|) e^{jn\angle I_{sc}(f)} \mathbf{E}_r(\mathbf{r}, \mathbf{r}_s, nf); \quad (9)$$

where $\ell_e(f)$ is the vector effective length of the scatterer and $\mathbf{E}_r(\mathbf{r}, \mathbf{r}_s, nf)$ is the radiated field pattern of the scatterer when excited with a unity voltage source. Also note that the structural mode for an extended target can be written as a superposition of responses from point-like scatterers. To obtain the most general treatment, the framework above can be expressed in terms of the dyadic Green's function for the vector field problem; nevertheless, it is seen that it is sufficient to evaluate the imaging functional (Eq. 5) by using the dominant field and Green's function components of interaction.

3. Numerical Experiments

Scattering and imaging simulations are performed in this section to illustrate the formalism established in the previous section.

3.1 Harmonic Scattering Characterization

The electromagnetic response of the scatterer is computed using a hybrid method-of-moments and harmonic balance approach, together with an asymptotic field propagator. The impedance of the scatterer $Z_s(f)$ and the short-circuit current at the scatterer terminal $I_{sc}(f)$ are first characterized in the spectral domain by applying the free-space and half-space mixed-potential integral equation solver.²⁹ Then—in the circuit domain—a harmonic balance technique¹⁴ is employed for obtaining the terminal voltage response $V_s(nf)$ of the target connected to the nonlinear load. In essence, after dividing the equivalent circuit for the scatterer into linear and nonlinear sections at the terminal reference plane and applying the standard nodal current law, a

nonlinear matrix system is established and subsequently solved with an iterative method. Finally, the resultant harmonic currents over the structure are deduced using the integral equation solver once again. Note that for the half-space problem, for the calculation of the dyadic and scalar Green's functions within the integral equation solver, exact Sommerfeld integrals are used. To increase the computational efficiency, a tabulation-and-interpolation routine is employed for evaluating these integrals. On the other hand, for field scattering and propagation, the second-order-accurate asymptotic approximations to the integrals are exploited instead;^{30,31} such a treatment allows the second-order surface wave component to be included in the solution. The overall simulation framework outlined above closely follows the one delineated previously,²⁶ where more details and formulations can be found.

3.2 Imaging Results and Discussions

A free-space, point-like target is examined first using the framework presented in the above sections. The target is a small vertical dipole element with length $l \ll \lambda_{\min}$, where λ_{\min} is the minimum wavelength over the harmonic frequency bands used for imaging. The dipole is center-loaded with a diode with $i(t) = I_o (\exp(v(t)/v_t) - 1)$, $I_o = 10$ nA, $v_t = 26$ mV. The sensing geometry is as illustrated in Fig. 1: the linear array is composed of 17 equally spaced elements distributed over a 2-m-wide aperture; the center of the array is at (10, 0, 2) m, with the target situated at the coordinate origin. A bistatic configuration employing a single illuminator is assumed: the illuminator—with transmitted power of 10 W at all incident frequencies and located at the center of the array—is a vertical infinitesimal electric dipole operating over the frequency band [300 MHz, 1.5 GHz] in $P = 401$ steps. For image generation, the scattered fields up to the fourth harmonic are collected for each frequency. (Here then λ_{\min} corresponds to the wavelength at frequency $4f_p$.) Fig. 2 shows $|\Psi_n(\mathbf{r})|$ for $n = 1, 2, 3, 4$. (The derived imaging theory can be applied to higher orders of n , of course, but for demonstration purposes, only the results for up to the fourth order are included in this work.) The Green's function $G(\cdot, \cdot, f)$ within Eq. 5 is calculated asymptotically with the previously derived formulations.^{30,31} The images are constructed without any spectral window and are seen to match the theoretical point spread function²⁸ very well, with the resolutions as predicted by Eqs. 6 and 7; the down-range and cross-range imaging sidelobe artifacts are also consistent with expectations. It should be noted that the re-radiated field $E_{s,r}(\mathbf{r}, \mathbf{r}', nf)$ is of the form $\propto f^{n+2}$ in the small-signal regime whereas the structural scattered mode $E_{s,0}(\mathbf{r}, \mathbf{r}', f)$ is $\propto f^2$ (Rayleigh scattering); these frequency dependencies—which can also be readily derived from Eqs. 2 and 4—have been compensated in generating the images in Fig. 2.

The imaging and scattering characteristics of on-surface and shallow-buried point-like targets are similar to those of the free-space case and therefore are not explicitly included here.

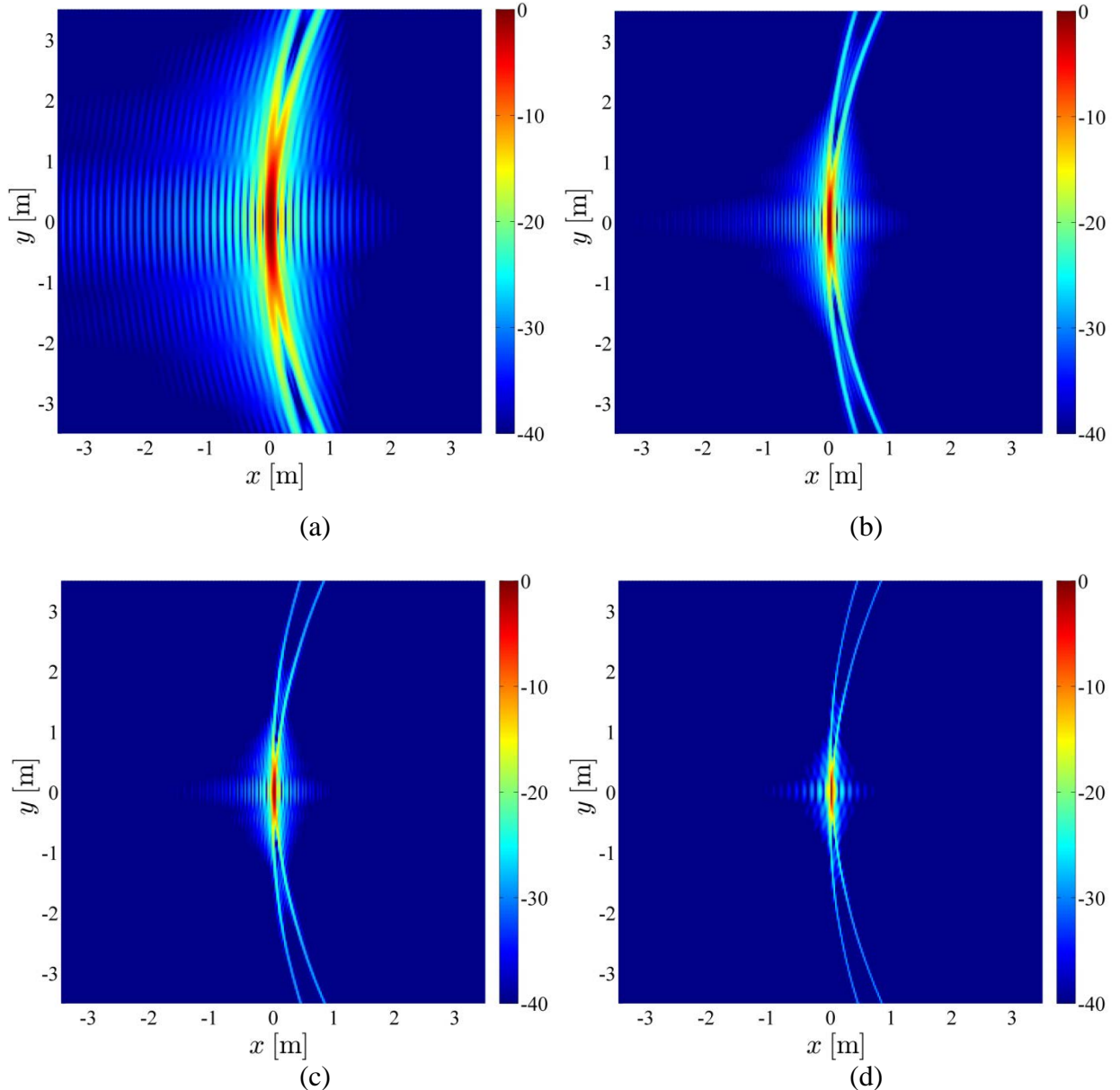


Fig. 2 Harmonic imaging results for diode-loaded, free-space point-like target: a) $|\Psi_1(\mathbf{r})|$; b) $|\Psi_2(\mathbf{r})|$; c) $|\Psi_3(\mathbf{r})|$; and d) $|\Psi_4(\mathbf{r})|$. $F = [300 \text{ MHz}, 1.5 \text{ GHz}]$, transmitted power = 10 W.

A nonlinearly loaded extended scatterer is considered next. The scatterer is a vertical dipole element of length $l = 0.5$ m, center-loaded with a diode; the parameters of the diode and the sensing configuration are the same as those described above. The time and frequency domain backscattering responses at the center array element for up to the fourth harmonic are displayed in Figs. 3–6 for the free-space, on-surface, and shallow-buried scenarios. The image domain

results corresponding to these scenarios are shown in Figs. 7–9. For the half-space problem, the ground soil has relative dielectric constant $\varepsilon_r = 4$ and conductivity $\sigma = 15$ mS/m, and the target is positioned directly on top of the surface or buried at 3 cm depth. For the time-domain signal reconstruction, the step-frequency-based excitation waveform is derived by taking the inverse Fourier transform of a Blackman spectral window. It is seen that, in these examples, the dominant contribution to the first-order harmonic return is provided by the structural mode scattering. As a result, at least according to the frequency-domain plots, the first-order harmonic response is quite dissimilar from the higher-order ($n > 1$) ones. The reverberations seen in the first-order harmonic time- and image-domain signals are due to single- and multiple-order diffractions from the ends of the dipole;^{32, 33} these diffraction effects are also noted for the higher-order harmonic signals, though they are not as well defined as those in the first-order harmonic case. (In general, a direct correspondence between the peaks of the time-domain signal and the maxima in the image may not be readily observable in these results because of the complicated diffraction effects; however, an approximate equivalence between the time and image domain responses does exist for free-space and above-ground targets: it can be shown that the time-domain response of a transmitter and receiver pair is twice the real part of the complex image response contribution due to that pair.)

As evident from Eqs. 8 and 9, note that the re-radiation mode is spectrally modulated by the radiation characteristics of the scatterer (as well as by the properties of the nonlinear loading). In these examples, the “shape” of each set of higher-order harmonic frequency domain responses in Fig. 6 is largely determined by the functions $\ell_e(f)$ and $E_r(\mathbf{r}, \mathbf{r}_s, nf)$ —the variations of both of which also reflect the resonance properties of the scatterer. This spectral modulation makes it difficult to identify a specific order of diffraction from the dipole ends in the higher-order harmonic time and image responses. For the free-space and above-ground target cases, the higher-order harmonic frequency-domain responses (Figs. 6a and 6b, for $n > 1$) are weaker over the second half of the band than over the first half since the main lobe of $\ell_e(f)$ for the vertical dipole—which occurs near the broadside direction (or near the plane of the ground) at the lower frequencies—shifts to higher elevation angles as the frequency increases toward 1.5 GHz; as such, the induced short-circuit current $I_{sc}(f)$ is reduced over the second half of the band, where the small-signal regime consequently occurs and, thus, the scattering signal intensity in general decreases with increasing harmonic number (i.e., $E_{s,r}(\mathbf{r}, \mathbf{r}', nf) \propto |I_{sc}(f)|^n$). For the buried-target case, as expected, the scattering signal intensities on average are much weaker as compared to those of the free-space and on-surface target cases, and the small-signal regime is applicable over the entire band. Note that the four principal local maxima observed here in the higher-order harmonic spectral responses (Fig. 6c) correspond to the resonance frequencies of $\ell_e(f)$.

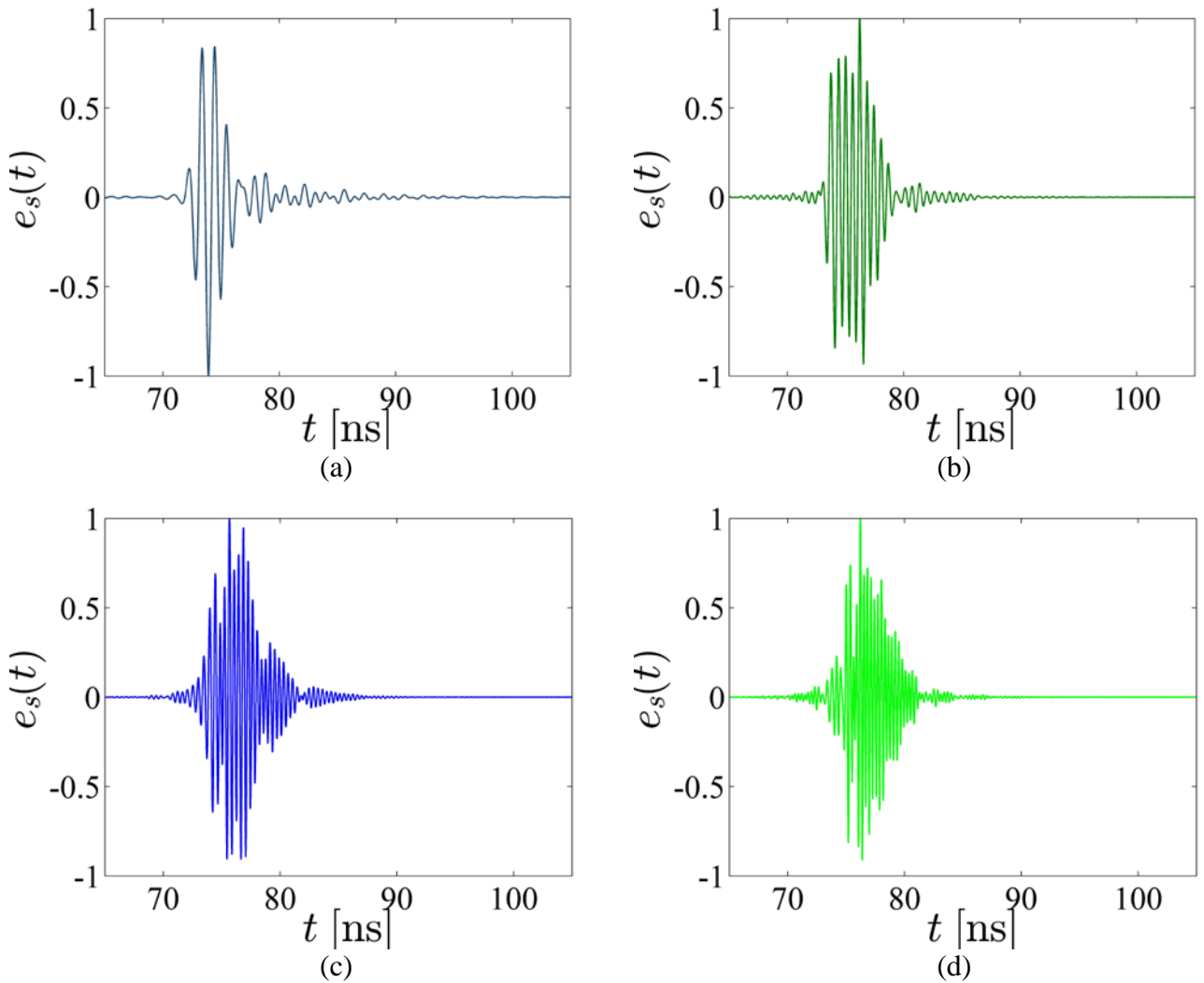


Fig. 3 Normalized time-domain harmonic scattering responses for diode-loaded, free-space extended target:
a) $n = 1$; b) $n = 2$; c) $n = 3$; and d) $n = 4$

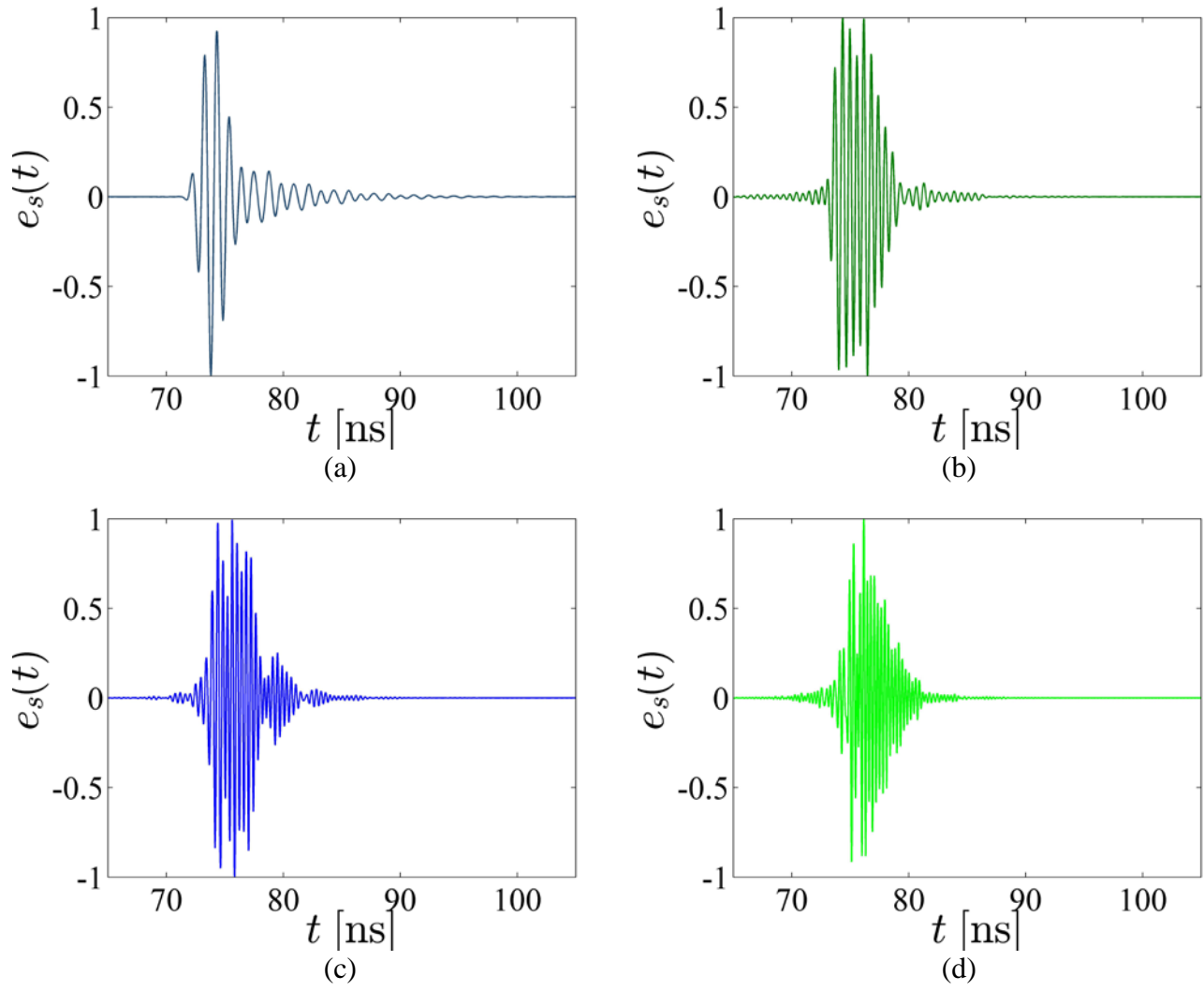


Fig. 4 Normalized time-domain harmonic scattering responses for diode-loaded, on-surface extended target:
a) $n = 1$; b) $n = 2$; c) $n = 3$; and d) $n = 4$

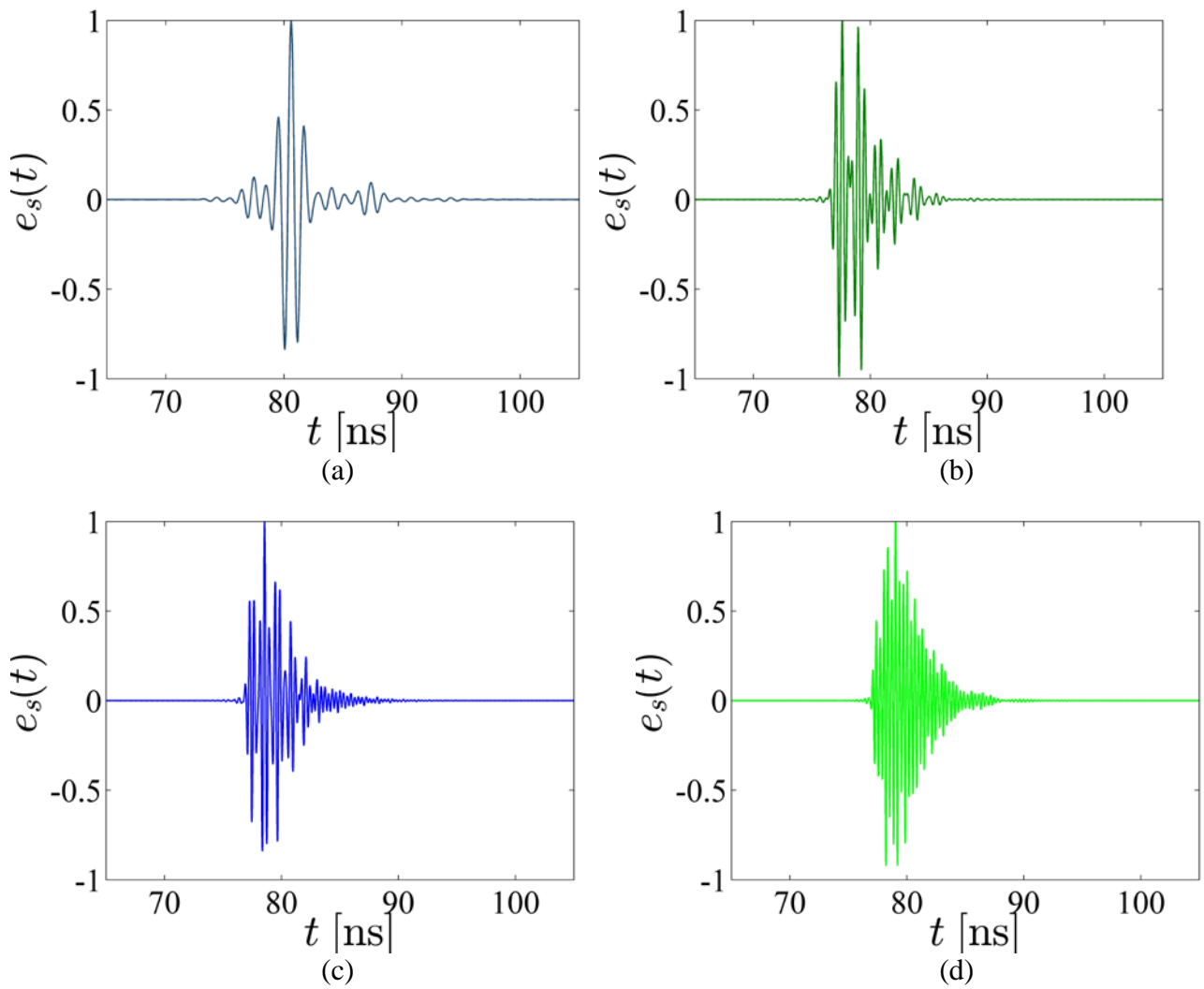


Fig. 5 Normalized time-domain harmonic scattering responses for diode-loaded, subsurface extended target:
a) $n = 1$; b) $n = 2$; c) $n = 3$; and d) $n = 4$

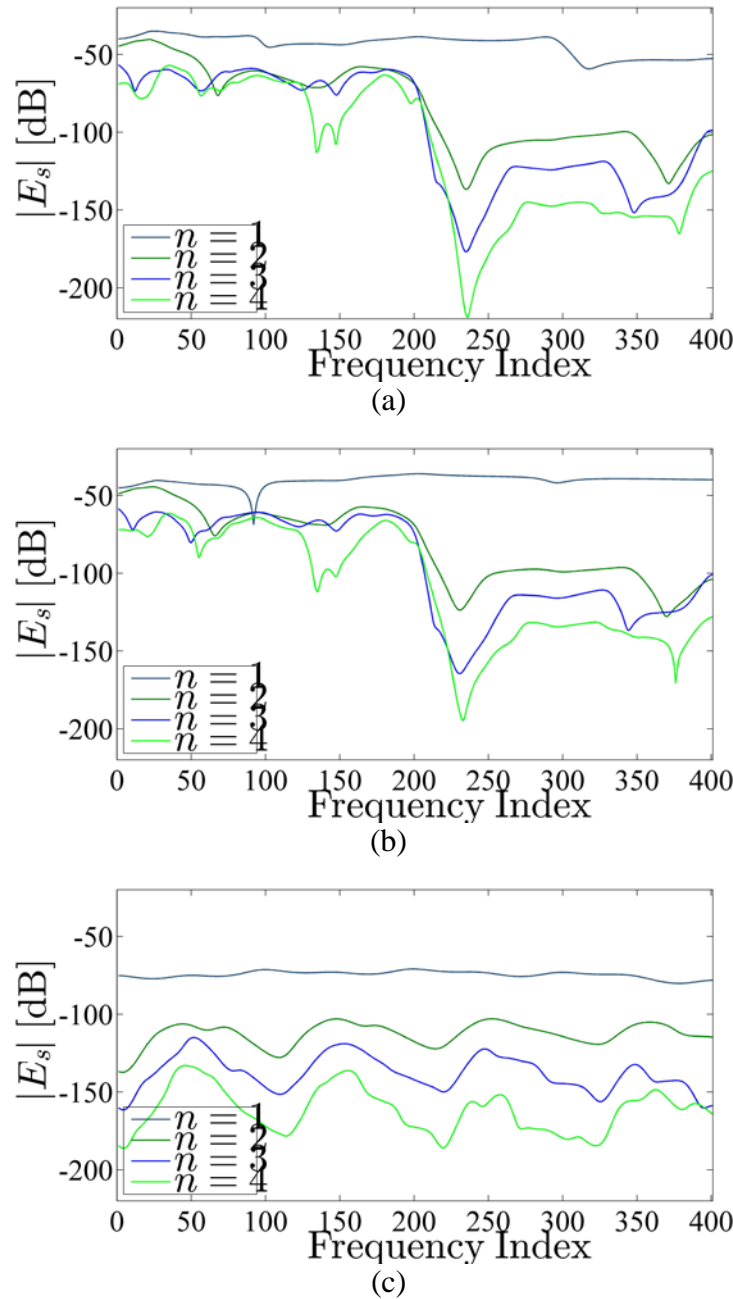


Fig. 6 Frequency-domain harmonic scattering responses for diode-loaded extended target for $n = 1,2,3,4$: a) free-space; b) on-surface; and c) subsurface

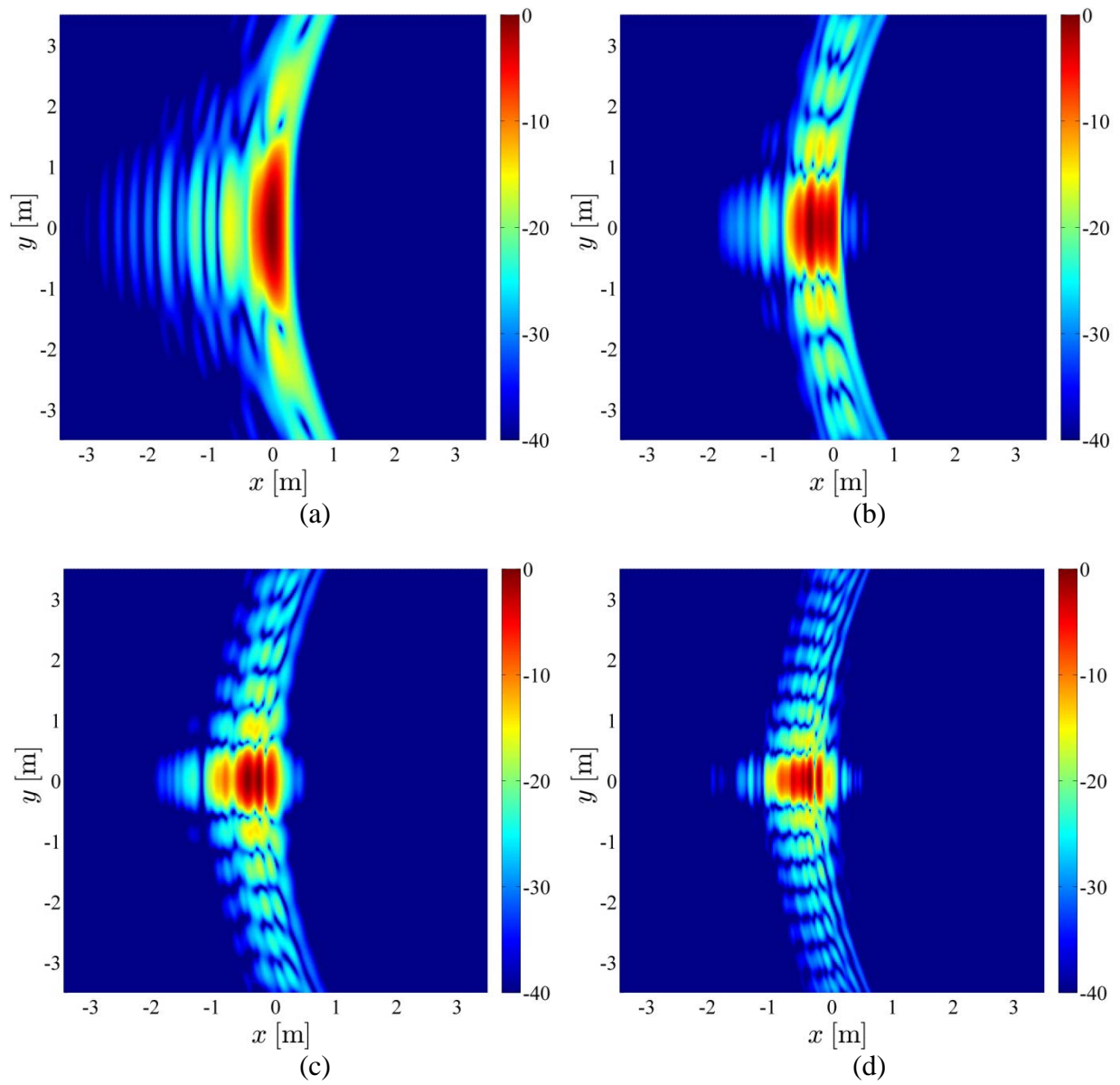


Fig. 7 Harmonic imaging results for diode-loaded, free-space extended target: a) $|\Psi_1(\mathbf{r})|$; b) $|\Psi_2(\mathbf{r})|$; c) $|\Psi_3(\mathbf{r})|$; and d) $|\Psi_4(\mathbf{r})|$. F = [300 MHz, 1.5 GHz], transmitted power = 10 W.

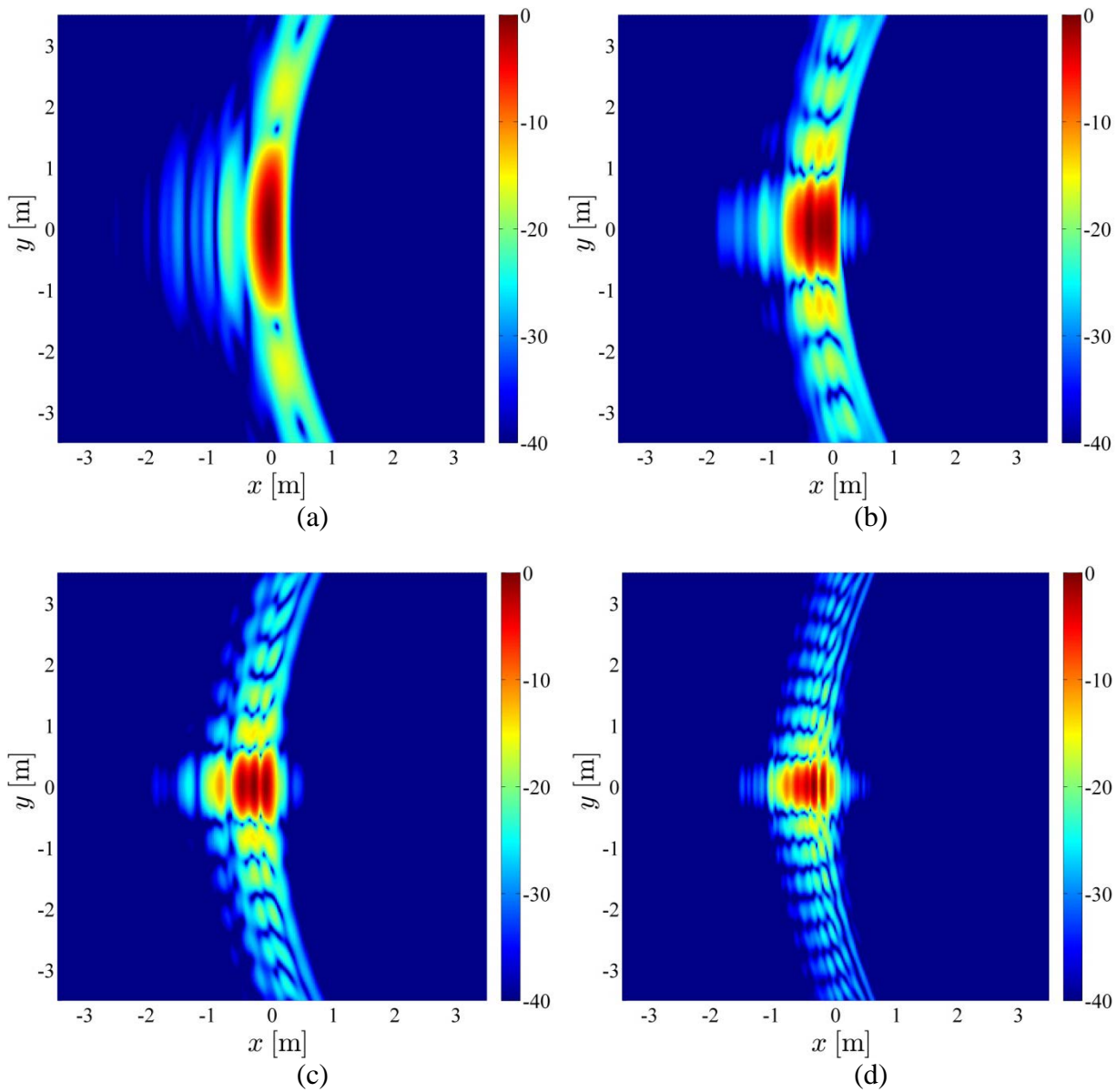


Fig. 8 Harmonic imaging results for diode-loaded, on-surface extended target: a) $|\Psi_1(\mathbf{r})|$; b) $|\Psi_2(\mathbf{r})|$; c) $|\Psi_3(\mathbf{r})|$; and d) $|\Psi_4(\mathbf{r})|$. $F = [300 \text{ MHz}, 1.5 \text{ GHz}]$, transmitted power = 10 W.

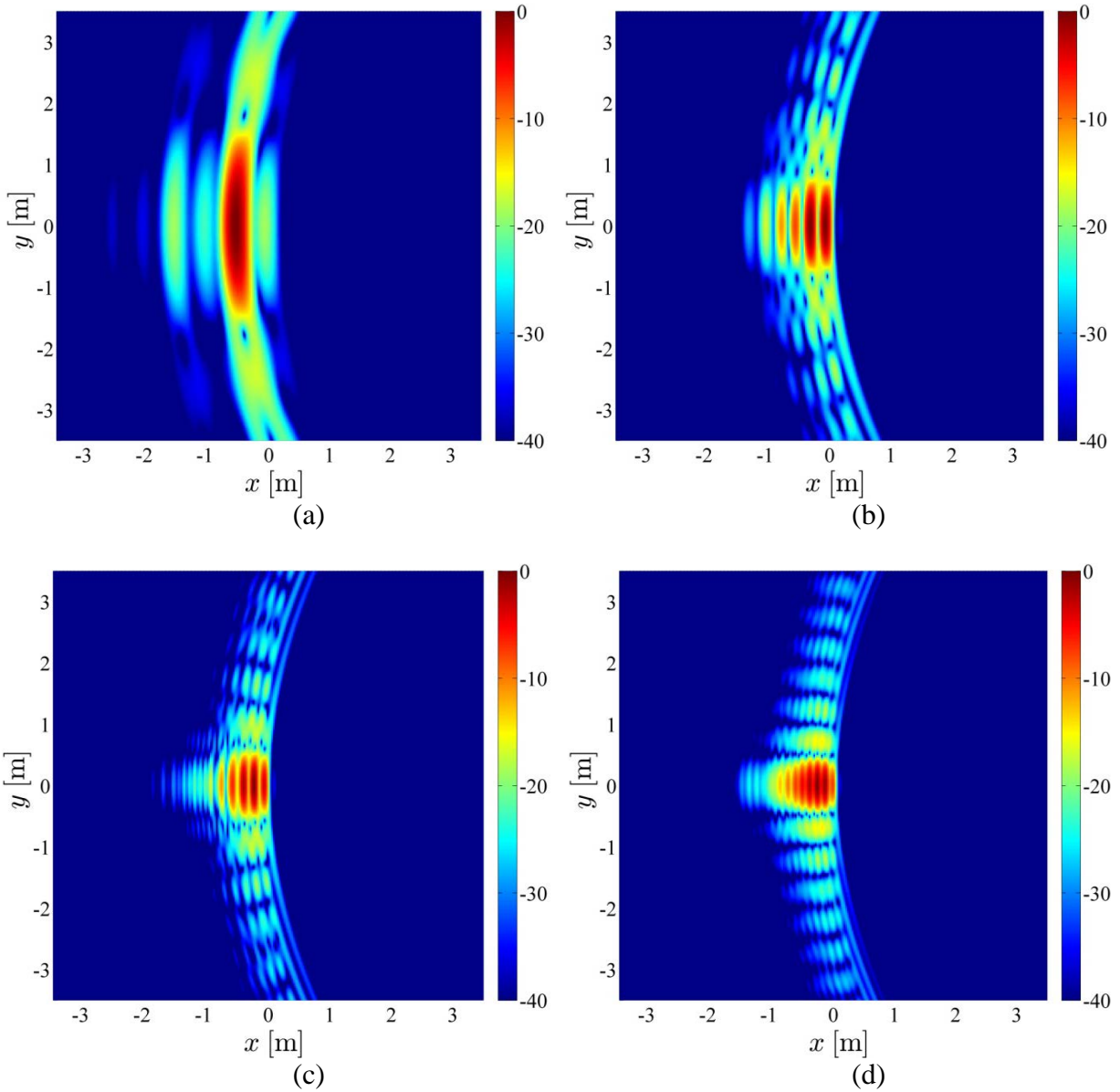


Fig. 9 Harmonic imaging results for diode-loaded, subsurface extended target: a) $|\Psi_1(\mathbf{r})|$; b) $|\Psi_2(\mathbf{r})|$; c) $|\Psi_3(\mathbf{r})|$; and d) $|\Psi_4(\mathbf{r})|$. $F = [300 \text{ MHz}, 1.5 \text{ GHz}]$, transmitted power = 10 W.

Although the full-band data are always processed to obtain the results in Figs. 7–9, the images can also be constructed with only sub-band data—that is, for instance, given that a stronger response is observed over the first half of the band for the free-space and above-ground cases, one may choose to generate the images using the signal only from that sub-band; this, of course, would lead to a loss in image resolution.

The standoff sensing method investigated herein is envisioned for use primarily in the short range. From asymptotic analysis, in the small-signal regime, it can be shown that the amplitude of the n -th harmonic backscattered field has a dependence of the form $\propto \rho^{-2(n+1)}$, where ρ is the radial distance from the transceiver to the scatterer. The faster propagation attenuation rate of the higher-order harmonic signal intensities as a function of distance requires high power to be transmitted for long range applications.

4. Conclusions

A wideband, step-frequency-based harmonic image construction method has been formulated for the localization of free-space and near-ground nonlinearly loaded scatterers. The nonlinear scattering theory in support of the method has been outlined. Numerical experiments have been carried out to demonstrate the underlining concepts appearing herein. First, the steady-state harmonic scattering responses from point-like and extended targets are characterized using a hybrid frequency-domain full-wave solver, in conjunction with a harmonic balance approach and an asymptotic propagation technique. Then, the harmonic signals are analyzed in the time, frequency, and image domains for targets in free-space and half-space environments. The numerical examples illustrate that the targets are accurately localized by employing a forward-looking bistatic sensing configuration consisting of a single transmitter and a linear array of receivers.

The overall analysis framework established in this study can be applied to investigate target scattering and imaging responses as a function of—for example—incident (or transmitted) power, frequency band of operation, standoff range, and sensing geometry. Although the mode of excitation of interest here is sequential single-tone illumination, the scattering algorithm and the imaging method are expected to be readily extendable to other modes of excitation, such as sequential double-tone and multiple-tone illumination over a wideband.

5. References

1. Kositsky J, Cosgrove R, Amazeen C, Milanfar P. Results from a forward-looking GPR mine detection system. Proc. SPIE. 2002;4038.
2. Bradley M, Witten T, Duncan M, McCummins B. Mine detection with a forward-looking ground-penetrating synthetic aperture radar. Proc. SPIE. 2003;5089.
3. Wang T, Sjahputera O, Keller JM. Landmine detection using forward-looking GPR with object tracking, Proc. SPIE. 2005;5794.
4. Ressler M, Nguyen L, Koenig F, Wong D, Smith G. The ARL synchronous impulse reconstruction (SIRE) forward-looking radar. Proc. SPIE. 2007;6561.
5. Wang J, Li Y, Zhou Z, Jin T, Yang Y, Wang Y. Image formation techniques for vehicle-mounted forward-looking ground-penetrating SAR. Intnl. Conf. Info. Automat. 2008.
6. Riley JR, Smith AD. Design considerations for an harmonic radar to investigate the flight of insects at low altitude. Comput. Electron. Agr. 2002;35:151–169.
7. Nikitin PV, Rao KVS. Harmonic scattering from passive UHF RFID tags. Proc. IEEE Antennas and Propagat. Soc. Symp. 2009.
8. Vera GA, Duroc Y, Tedjini S. RFID test platform: Nonlinear characterization. IEEE Trans. Instrum. M. 2014.
9. Schuman HK. Time-domain scattering from a nonlinearly loaded wire. IEEE Trans. Antennas Propagat. 1974;22:611–613.
10. Liu TK, Tesche FM. Analysis of antennas and scatterers with nonlinear loads. IEEE Trans. Antennas Propagat. 1976;24:131–139.
11. Sarkar TK, Weiner DD, Harrington RF. Analysis of nonlinearly loaded multiport antenna structures over an imperfect ground plane using the Volterra-series method. IEEE Trans. Electromagn. Compat. 1978;20:278–287.
12. Kanda M. Analytical and numerical techniques for analyzing an electrically short dipole with a nonlinear load. IEEE Trans. Antennas Propagat. 1980;28:71–78.
13. Landt JA, Miller EK, Deadrick FJ. Time domain modeling of nonlinear loads. IEEE Trans. Antennas Propagat. 1983;31:121–126.

- 14 Huang C-C, Chu T-H. Analysis of wire scatterers with nonlinear or time-harmonic loads in the frequency domain. *IEEE Trans. Antennas Propagat.* 1993;41:25–30.
- 15 Luebbers R, Beggs J, Chamberlin K. Finite difference time domain calculation of transients in antennas with nonlinear loads. *IEEE Trans. Antennas Propagat.* 1993;41:566–573.
- 16 Porti JA, Morente JA. A numerical analysis of wire antennas loaded with varistor-composite materials. *IEEE Trans. Electromagn. Compat.* 1994;36:23–31.
- 17 Gorbachev AA, Zaboronkova TM, Tarakankov SP, Vasenkov AA. Scattering of electromagnetic waves by metallic thin antennas with a nonlinear local load. *Electromagnetics* 1998;18:439–452.
- 18 Lee KC. An efficient algorithm for the steady-state analysis of a nonlinearly loaded antenna array. *J. Electromagn. Waves Applicat.* 2000;14:1373–1382.
- 19 ——. Analysis of large nonlinearly loaded antenna arrays under multitones excitation. *Microw. Opt. Technol. Lett.* 2000;25:319–323.
- 20 ——. Two efficient algorithms for the analyses of a nonlinearly loaded antenna and antenna array in the frequency domain. *IEEE Trans. Electromagn. Compat.* 2000;45:339–346.
- 21 ——. Genetic algorithms based analyses of nonlinearly loaded antenna arrays including mutual coupling effects. *IEEE Trans. Antennas Propagat.* 2003;51:776–781.
- 22 Poljak D, Tham CY, McCowen A. Transient response of nonlinearly loaded wires in a two media configuration. *IEEE Trans. Electromagn. Compat.* 2004;46:121–125.
- 23 Sheshyekani K, Sadeghi SHH, Moini R. A combined MoM-AOM approach for frequency domain analysis of nonlinearly loaded antennas in the presence of a lossy ground. *IEEE Trans. Antennas Propagat.* 2008;56:1717–1724.
- 24 Ostadzadeh SR, Tayarani M, Soleimani M. A hybrid model in analyzing nonlinearly loaded dipole antenna and finite antenna array in the frequency domain. *Int. J. RF and Microwave Comp. Aid Eng.* 2009;19:512–518.
- 25 Karami HR, Moini R, Sadeghi SHH, Sheshyekani K. Transient response of nonlinearly loaded antennas above a lossy dielectric half-space: A modified MoM-AOM approach. *IEEE Trans. Electromagn. Compat.* 2012;54:922–930.
- 26 Liao DH. Scattering and imaging of nonlinearly loaded antenna structures in half-space environments. *IEEE Trans. Antennas Propagat.* 2014;62:1–11, accepted, to be published (<http://dx.doi.org/10.1109/TAP.2014.2322875>).

27 Sinclair G. The transmission and reception of elliptically polarized waves. Proc. I.R.E. 1950.

28 Liao DH, Dogaru T, Sullivan A. Large-scale, full-wave-based emulation of step-frequency forward-looking radar imaging in rough terrain environments. *Sens. Imaging* 2014;15:1–29.

29 Liao DH, Sarabandi K. Terminal-to-terminal hybrid full-wave simulation of low-profile, electrically-small, near-ground antennas. *IEEE Trans. Antennas Propagat.* 2008;56:806–814.

30 ——. Near-earth wave propagation characteristics of electric dipole in presence of vegetation or snow layer. *IEEE Trans. Antennas Propagat.* 2005;53:3747–3756.

31 Liao DH. Physics-based near-earth radiowave propagation modeling and simulation. Ph.D. dissertation, The University of Michigan, 2009.

32 Shamansky HT, Daminek AK, Peters L. Electromagnetic scattering by a straight thin wire. *IEEE Trans. Antennas Propagat.* 1989;37:1019–1025.

33 Vitebskiy S, Carin L. Moment-method modeling of short-pulse scattering from and the resonances of a wire buried inside a lossy, dispersive half-space. *IEEE Trans. Antennas Propagat.* 1995;43:1303–1312.

1 DEFENSE TECHNICAL
(PDF) INFORMATION CTR
only) DTIC OCA

2 DIRECTOR
(PDF) US ARMY RESEARCH LAB
RDRL CIO LL
IMAL HRA

1 GOVT PRNTG OFC
(PDF) A MALHOTRA

4 DIRECTOR
(PDF) US ARMY RESEARCH LAB
RDRL SER U
D LIAO
T DOGARU
K SHERBONDY
A SULLIVAN